

Strongly pinned skyrmionic bubbles and higher-order nonlinear Hall resistances at the interface of Pt/FeSi bilayer

T. Hori ^{1,2} N. Kanazawa ^{1,*} K. Matsuura ^{3,4} H. Ishizuka,⁴ K. Fujiwara ⁵ A. Tsukazaki,⁵ M. Ichikawa ²
M. Kawasaki,^{2,3} F. Kagawa,^{3,4} M. Hirayama,^{2,3} and Y. Tokura^{2,3,6}

¹*Institute of Industrial Science, University of Tokyo, Tokyo 153-8505, Japan*

²*Department of Applied Physics, University of Tokyo, Tokyo 113-8656, Japan*

³*RIKEN Center for Emergent Matter Science (CEMS), Wako 351-0198, Japan*

⁴*Department of Physics, Tokyo Institute of Technology, Tokyo 152-8550, Japan*

⁵*Institute for Materials Research, Tohoku University, Sendai 980-8577, Japan*

⁶*Tokyo College, University of Tokyo, Tokyo 113-8656, Japan*



(Received 24 October 2023; accepted 4 April 2024; published 23 April 2024)

Engineering of magnetic heterostructures for spintronic applications has entered a new phase, driven by the recent discoveries of topological materials and exfoliated van der Waals materials. Their low-dimensional properties can be dramatically modulated in designer heterostructures via proximity effects from adjacent materials, thus enabling the realization of diverse quantum states and functionalities. Here we investigate spin-orbit-coupling proximity effects of Pt on the recently discovered quasi-two-dimensional ferromagnetic state at the FeSi surface. Skyrmionic bubbles (SkBs) are formed as a result of the enhanced interfacial Dzyaloshinsky-Moriya interaction. The strong pinning effects on the SkBs are evidenced from the significant dispersion in size and shape of the SkBs and are further identified as a greatly enhanced threshold current density required for depinning of the SkBs. The robust integrity of the SkB assembly leads to the emergence of higher-order nonlinear Hall effects in the high current density regime, which originate from nontrivial Hall effects due to the noncollinearity of the spin texture, as well as from the current-induced magnetization dynamics via the augmented spin-orbit torque.

DOI: [10.1103/PhysRevMaterials.8.044407](https://doi.org/10.1103/PhysRevMaterials.8.044407)

I. INTRODUCTION

Atomically thin magnets and their heterostructures offer an excellent platform for realizing a variety of spin states and spintronic functionality [1–4]. The recent energetic exploration of magnetic or magnetically proximitized topological materials [5–8] and van der Waals materials [9–13] pushes the frontier as highlighted in the realization of the quantum anomalous Hall effect [14–17] and the advances in valleytronics applications [18,19]. Simply because a small number of carriers and spins are involved in the ultrathin films, the magnetic states are responsive to external stimuli such as electric currents and gate voltages or are susceptible to extrinsic effects such as defects and surface roughness. This enables us to control their spintronic functionalities in various ways, while dramatically reducing the energy consumption.

In addition to the low dimensionality, structural symmetry breaking is particularly important for emergent phenomena induced by spin-orbit coupling (SOC) in the ultrathin films [20–23]. As a consequence of the broken inversion symmetry at the surfaces or interfaces, antisymmetric SOC effects arise, such as the Rashba effect [24] and the Dzyaloshinsky-Moriya (DM) interaction [25,26]. Their antisymmetric nature leads

to the formation of rich spin textures in momentum spaces and real spaces, i.e., spin-momentum locking in energy bands [20,23] and Néel-type domain walls and skyrmions [27–29]. The interplay between the conduction electrons and those spin textures causes various transport phenomena, to name a few, the Edelstein effect [30], spin-orbit torques (SOTs) [31,32], nonreciprocal transports of the second order in the electric field E [33,34], the topological Hall effect [35,36], and skyrmion drive [37,38].

The recently discovered ferromagnetic surface of the chiral-lattice FeSi constitutes a new form of quasi-two-dimensional (2D) magnetic state [39,40]. While the bulk interior of FeSi is of a nonmagnetic insulating state [41], multiple experimental techniques have revealed that its surface exhibits both conductive (metallic) behaviors [39,40,42–44] and ferromagnetic ordering [39,40]. Here the ferromagnetic order is confined within a depth of ~ 3.5 Å from the surface, which corresponds approximately to the top three surface-Fe layers [39]. Polar distribution of surface electronic orbitals, which is characterized by the quantized Zak phase [45] or the topology of electric polarization [46–48], boosts the potential gradient perpendicular to the surface and results in large Rashba spin splitting (~ 35 meV) [39] despite the relatively low atomic numbers of Fe and Si. Owing to the coexistence of the ferromagnetic-metal properties and the large Rashba SOC at the surface, SOT-induced magnetization switching is realized even at room temperature without external assist

* Author to whom correspondence should be addressed:
naoya-k@iis.u-tokyo.ac.jp

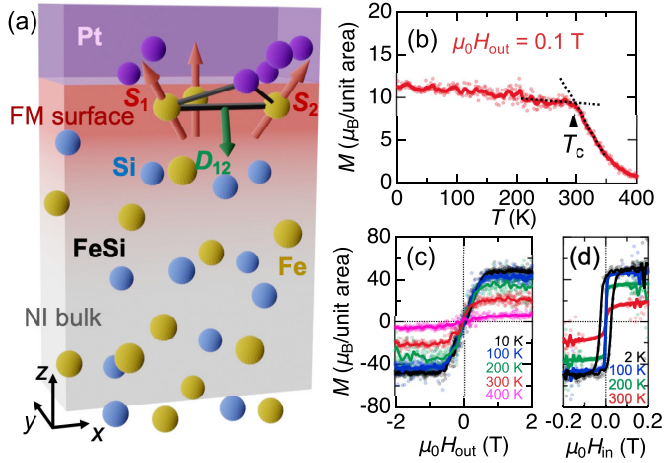


FIG. 1. Magnetic properties at the interface between Pt ($t = 3$ nm) and FeSi ($t = 5$ nm). (a) Schematic picture of the Pt/FeSi bilayer. As a consequence of the spin-orbit-coupling (SOC) proximity of Pt, the interfacial Dzyaloshinsky-Moriya (DM) interaction twists the spins at the ferromagnetic-metal (FM) surface of FeSi with the nonmagnetic-insulating (NI) bulk, inducing noncollinear spin textures. Here D_{12} represents the DM vector acting on spins S_1 and S_2 . (b) Temperature dependence of the magnetization M under an out-of-plane magnetic field $\mu_0 H_{\text{out}} = 0.1$ T. The kink around $T = 295$ K represents the helimagnetic ordering. (c) and (d) Out-of-plane and in-plane magnetic-field dependence of magnetization at various temperatures. The measured data (color dots) are smoothed (color lines) for clarity. The unit area corresponds to $\sqrt{3}a^2$, where a is the lattice constant of the cubic unit cell of FeSi.

magnetic fields [40]. Here we note that there are other arguments for topological aspects of the FeSi surface state in terms of topological Kondo insulators [42] or Weyl semimetals [49], partly because the origin of the bulk band gap still remains an interesting question [50–53].

In this article, we explore spintronic properties at the FeSi surface by fabricating an interface with Pt and leveraging the intrinsically strong SOC through proximity effects. The enhanced DM interaction facilitates the formation of skyrmionic bubbles (SkBs) at the ferromagnetic interface [Fig. 1(a)], where they undergo a strong pinning effect from inherent structural disorders. The simultaneous confinement of conduction electrons and SkBs within the 2D interface offers a unique platform for examining their interplay through SOC by standard electrical transport measurements, which have not been feasible on mono- or bi-atomic-layer interfaces segmented into islands of tens of nanometers in size [54,55]. Here we find higher-order nonlinear Hall effects, extending up to the seventh order, in the high current density regime, indicating an unconventional mechanism of asymmetric electron scatterings by the noncollinear spin structure of SkBs.

II. METHODS

The Pt/FeSi bilayer was fabricated on an insulating Si(111) substrate in an *in situ* setup combining molecular beam epitaxy (MBE) and sputtering methods. While the FeSi(111) layer with thickness $t = 5$ nm was epitaxially grown on the Si substrate by MBE [56], the Pt layer with

$t = 3$ nm was deposited at room temperature by sputtering. Also see Refs. [39,40] for the detailed growth procedures. The epitaxial growth of FeSi was confirmed by the θ - 2θ x-ray diffraction method, while the surface roughness was estimated by atomic force microscopy (AFM) (Supplemental Material [57], Fig. S1). The thin-film sample was processed into Hall-bar devices of 30- μm width and 40- μm length by using UV lithography and Ar ion milling. The Hall-bar devices were connected to electrodes made of Au (45 nm)/Ti (5 nm) by electron beam deposition.

Magnetization measurements were performed by using the reciprocating sample option of a magnetic property measurement system (MPMS, Quantum Design). Hall resistance measurements were performed by using a lock-in technique (SR-830, Stanford Research Systems), where higher-order harmonic Hall voltages up to the seventh order in response to an input of ac current were measured.

Frequency-modulated magnetic force microscopy (MFM) was performed in noncontact mode with a lift height of 160 nm in a commercially available scanning probe microscope (AFM/MFM I, attocube) on a Hall-bar device. We used the MFMR tip (supplied by NANOSENSORS). Electric current pulses were injected into the Hall-bar device before each MFM scan for evaluating the magnetic domain response to the current.

III. RESULTS AND DISCUSSION

Magnetization (M) measurements revealed that the interfacial state shows ferromagnetic behaviors with in-plane anisotropy below the ordering temperature $T_c \approx 295$ K [Figs. 1(b)–1(d)]. Here we convert the magnetization size to a value per unit area of the FeSi(111) surface. (The unit area corresponds to $\sqrt{3}a^2$, where a is the lattice constant of the cubic unit cell of FeSi.) The magnetization size gradually grows with decreasing temperature T and subsequently undergoes little variation below T_c under an out-of-plane magnetic field $\mu_0 H_{\text{out}} = 0.1$ T [Fig. 1(b)]. The magnetization increases linearly with H_{out} below the saturation field H_c [Fig. 1(c)], while it shows a clear hysteresis loop under a cyclic variation in the in-plane magnetic field H_{in} [Fig. 1(d)]. These anisotropic responses of M indicate that the interfacial ferromagnetic moments tend to align in the film plane, in contrast to the perpendicular anisotropy observed at the FeSi interfaces with insulating oxides or fluorides [39,40]. The change in the easy direction of M indicates the variation in the magnitude and the direction of the orbital magnetic moment [58,59], which can be ascribed to reconstruction of the d -orbital occupancy of the FeSi surface state through the electronic hybridization with the Pt layer. We also note that the degree of the interlayer hybridization dramatically affects the magnetic transition temperature through modulating the density of states around the Fermi energy [40]. In particular, the chemical stability of Pt with the nearly filled d orbitals and the consequent low degree of hybridization may underlie the generation of the high T_c .

To further investigate the detailed magnetic structure and its responses to electric currents, we performed MFM imaging of a Hall-bar patterned Pt/FeSi under various H_{out} at $T = 10.8$ K [Fig. 2(a)]. Here the spatial modulation of out-of-plane

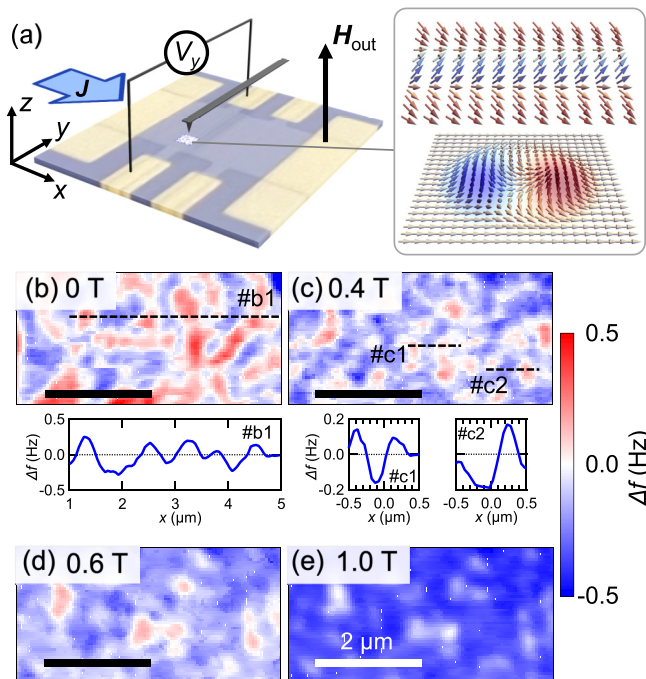


FIG. 2. Magnetic force microscopy (MFM) imaging of the Hall-bar patterned Pt/FeSi bilayer under out-of-plane magnetic fields H_{out} at $T = 10.8$ K. (a) Experimental setup for MFM imaging. The Au/Ti electrode pads (yellow regions) are used for the injection of current pulses and the detection of Hall voltages. Inset shows schematic illustrations of the expected magnetic structures, i.e., a transverse-conical state (cycloidal spin modulation with an in-plane ferromagnetic component) and a skyrmionic-bubble state (bimeron in an in-plane magnetization background). (b)–(e) MFM images at $\mu_0 H_{\text{out}} = 0$ T (b), 0.4 T (c), 0.6 T (d), and 1.0 T (e). No current pulses were applied before taking the MFM images. The line scans along #b1, #c1, and #c2 (dashed lines) are shown in the insets of panels (b) and (c). The scale bars represent $2 \mu\text{m}$.

M_z , i.e., the local M_z component, was detected as a frequency change Δf of the vibrating cantilever magnetized along H_{out} .

An intricate pattern comprising isolated magnetic domains of various sizes and shapes is observed at $\mu_0 H_{\text{out}} = 0$ T, ranging from submicrometer-scale circular bubbles to micrometer-scale island domains [Fig. 2(b)]. Under the application of $\mu_0 H_{\text{out}} = 0.4$ T, these domains undergo fragmentation, resulting in a disordered assembly of irregularly shaped bubble domains [Fig. 2(c)]. The number of these domains decreases with increasing H_{out} [Fig. 2(d) for $\mu_0 H_{\text{out}} = 0.6$ T] and finally disappear above H_c [Fig. 2(e) for $\mu_0 H_{\text{out}} = 1.0$ T]. The residual contrast observed at $\mu_0 H_{\text{out}} = 1.0$ T [Fig. 1(e)] is attributed to the structural roughness at the surface [Supplemental Material [57], Fig. S1(b)], since no change in the image was discerned even at $\mu_0 H_{\text{out}} = 4.0$ T (not shown). The domain width is roughly 500 nm as evaluated from the line scans in Figs. 2(b) and 2(c).

By analogy with the formation of spiral or skyrmionic spin textures commonly found in many heterostructures of ferromagnetic metals and heavy elements [27,28,60], the observed submicron domains are likely to originate from the interfacial DM interaction, which should be significantly enhanced by

the intrinsically strong SOC of Pt [61,62]. On the other hand, given the in-plane magnetic anisotropy in the Pt/FeSi bilayer, the magnetic domains would host different internal spin structures from the conventional cycloidal spin modulations or Néel-type skyrmions formed in the background of perpendicular magnetization. Although the in-plane spin arrangement cannot be determined in the present MFM setup, the observed domains may be highly deformed variants of transverse conical states [63] and bimerons [64–67] [see the inset of Fig. 2(a) for their schematic illustrations]. These postulated magnetic domains are in line with the oscillation profiles observed in the line scans [Fig. 2(c), #c1 and #c2].

The emergence of such noncollinear spin structures may be attributed to the DM vector \mathbf{D}_{ij} with an out-of-plane component [65]. The direction of the \mathbf{D}_{ij} vector is crucially dependent on the atomic arrangements at the interface as dictated by Moriya's rule [26] and consequently determines the twisting pattern of neighboring spins (\mathbf{S}_i and \mathbf{S}_j) as evident from the expression of DM interaction [$H_{\text{DM}} = \mathbf{D}_{ij} \cdot (\mathbf{S}_i \times \mathbf{S}_j)$]. The formation of bimeron-type magnetic domains indicates a different atomic stacking pattern at the Pt/FeSi interface and hence a distinct geometry of DM vectors, compared to the conventional multilayer films. These differences may stem from the characteristic chiral lattice structure of FeSi. The elucidation of the three-dimensional spin configuration and the interfacial crystal structure remains a future challenge for unraveling the formation mechanism of the complex spin texture. Hereafter, the isolated magnetic domains with noncollinear spin arrangements are collectively referred to as SkBs.

The observed features of magnetic domains, including the substantial dispersion in size and shape of SkBs and their disordered arrangements and zero-field metastability, indicate the presence of underlying structural disorders. These disorders include defects, surface roughness, and grain boundaries, which produce spatial fluctuations of magnetic interactions and anisotropy and hence a nonflat energy landscape for magnetic domains [68–70]. In fact, the consequent strong pinning effects are observed as robust immobility of magnetic domains against electric currents (Fig. 3). We injected successive three-current pulses with a duration of 10 ms at intervals of 1 s into the Hall bar and subsequently took a MFM image [Figs. 3(a), 3(b), 3(d), and 3(e)]. The current-induced changes in the magnetic-domain pattern were evaluated as the difference between MFM images with opposite current polarities [Figs. 3(c) and 3(f)]. Here the pulse current density J is calculated assuming that the current flows homogeneously through the device (cf. Supplemental Material [57], Fig. S2).

There is little change in the magnetic domain pattern in response to the application of $|J| \sim 1.5 \times 10^{11}$ A/m² [Figs. 3(a)–3(c)]. For the higher current pulses $|J| \sim 2.5 \times 10^{11}$ A/m², distinct transformations are spotted at various regions of the MFM image [Figs. 3(d)–3(f)], while no more variations can be induced by further injection of current pulses (Supplemental Material [57], Fig. S3). These results represent that a fraction of magnetic domains are selectively driven perhaps in a manner dependent on the strength of the pinning force and are subsequently trapped at the strong pinning sites like grain boundaries. Interestingly, the domain pattern can be repeatedly and reproducibly alternated between the

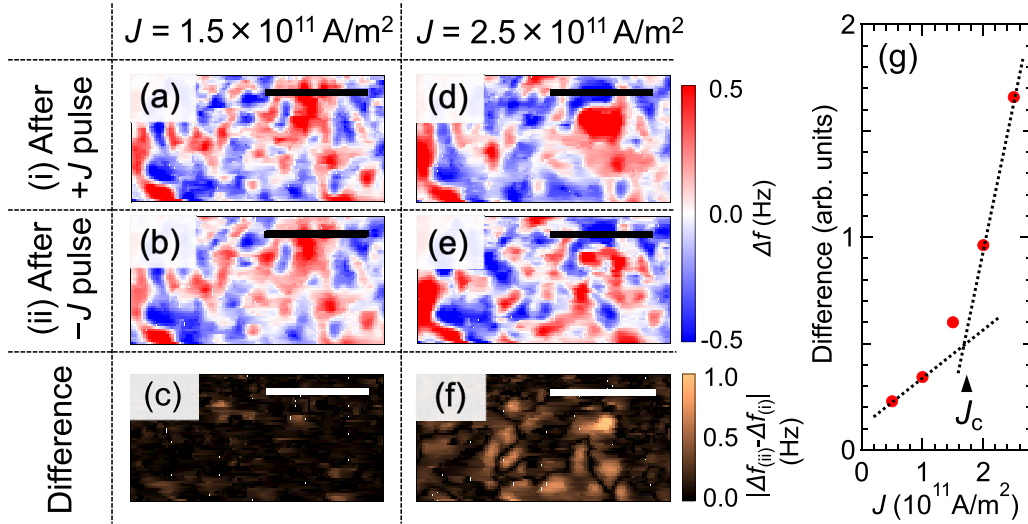


FIG. 3. Current-induced changes in the magnetic domain pattern at zero magnetic field. (a) and (b) Magnetic force microscopy (MFM) images after the injection of the pulse train (i.e., successive three-current pulses with current density $J = 1.5 \times 10^{11}$ A/m², with a duration of 10 ms, and at intervals of 1 s) in the positive (a) and negative (b) directions. (c) Difference between the MFM images [panels (a) and (b)] with the opposite current polarities. (d)–(f) MFM images [panels (d) and (e)] and difference image [panel (f)] in the case of the higher current density $J = 2.5 \times 10^{11}$ A/m². The scale bars represent 2 μ m. (g) Current density J dependence of the total difference integrated over the scanned area. The typical threshold current density J_c is estimated as the intersection of the dashed lines.

distinct trapped states [e.g., Figs. 3(d) and 3(e) for $J = \pm 2.5 \times 10^{11}$ A/m²] by reversing the current polarity (Supplemental Material [57], Fig. S3). This may be because the strong pinning sites are closely distributed at micrometer-scale intervals and effectively constrain the random diffusion of SkBs. The reversible nature also indicates that thermal or heating effects on the magnetic domain's motion play a secondary role, as these effects should be independent of the current polarity.

The total difference, i.e., the integrated value over each difference image, shows an accelerated rise with J [Fig. 3(g)], rather than an abrupt upturn across the threshold current density J_c . This continuous change with J also corroborates the local variations in the pinning potential, which lead to an expansion of the spectrum of threshold values. Nevertheless, the average J_c for depinning the domains can be approximated as 1.7×10^{11} A/m² [Fig. 3(g)]. The estimated J_c is several orders of magnitude larger than those for conventional skyrmions [37,71–73] and ranks among the highest reported values [38,74,75]. The greatly enhanced J_c can be partially attributed to the reduced dimensionality of this interfacial magnetic order; this aligns with theoretical predictions that suggest an inverse relationship between J_c and the thickness of magnetic layer [76,77].

The strong pinning effects at the Pt/FeSi interface enable us to investigate Hall transport properties in the SkBs without causing their displacement or disruption under a high current below the threshold value ($I < I_c$). Here we focus on the nonlinear Hall effects, motivated by the burgeoning interest in the nonlinear electromagnetic responses for their potential as novel quantum functionalities. Specifically, the nonreciprocal electrical conduction of the second order enable the rectification of current flows as represented by the recent discovery of superconducting diodes [78,79], while the highly nonlinear

magneto-transport properties constitute the fundamental element of physical reservoir computing [80–83].

The nonlinear Hall signals are typically enhanced in the high- I regime, in accord with their definition:

$$V_y = \sum_n R_{yx}^{(n)} I^n, \quad (1)$$

where $R_{yx}^{(n)}$ is the n th nonlinear Hall resistance. We evaluated $R_{yx}^{(n)}$ ($1 \leq n \leq 7$) by measuring higher-order harmonic Hall resistances $R_{yx}^{(nf)}$ in response to an input of harmonic ac current $I = I_0 \sin(2\pi ft)$. There is a direct relationship between $R_{yx}^{(n)}$ and $R_{yx}^{(nf)}$, which can be mathematically deduced in the low-frequency limit (see Supplemental Material [57]). The important point is that the even-order $R_{yx}^{(n)}$ is detected as the imaginary (out-of-phase) part of $R_{yx}^{(nf)}$; the odd-order $R_{yx}^{(n)}$ is detected as the real (in-phase) part of $R_{yx}^{(nf)}$. For example, the relationships for the second and third orders are expressed as follows:

$$\text{Im}[R_{yx}^{(2f)}] = -R_{yx}^{(2)} I_0 / 2, \quad (2)$$

$$\text{Re}[R_{yx}^{(3f)}] = -R_{yx}^{(3)} I_0^2 / 4. \quad (3)$$

Figures 4(a)–4(d) show H_{out} dependence of real and imaginary parts of $R_{yx}^{(nf)}$ ($n = 1, 2, 3$, and 5) at $T = 10$ K under the input ac current with $I_0 = 30$ mA (i.e., $|J| \leq 1.25 \times 10^{11}$ A/m²) and $f = 111$ Hz. (See Supplemental Material [57], Fig. S4 for other $R_{yx}^{(nf)}$.) The linear response $R_{yx}^{(1f)}$ represents a conventional anomalous Hall resistance in proportion to the out-of-plane component of M (i.e., M_z) [Fig. 4(a)] and also see Fig. 1(c). In contrast, the higher-order harmonic $R_{yx}^{(nf)}$, while being of significantly smaller magnitude as compared to $R_{yx}^{(1f)}$ [Fig. 4(f)], exhibit distinctive features that deviate from

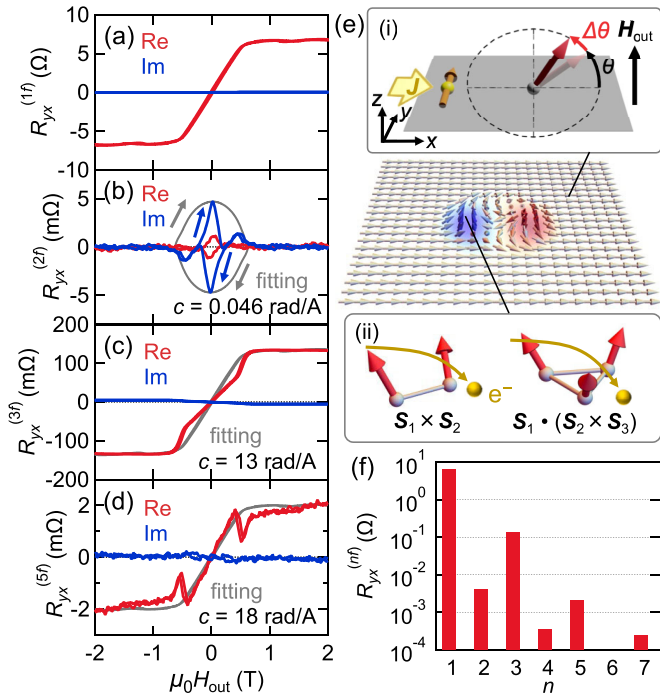


FIG. 4. Fundamental $R_{yx}^{(1f)}$ and higher-order harmonic $R_{yx}^{(nf)}$ Hall resistances in response to the ac current $I = I_0 \sin(2\pi ft)$ ($I_0 = 30$ mA and $f = 111$ Hz). (a)–(d) Out-of-plane magnetic-field H_{out} dependence of fundamental $R_{yx}^{(1f)}$ (a), second-harmonic $R_{yx}^{(2f)}$ (b), third-harmonic $R_{yx}^{(3f)}$ (c), and fifth-harmonic $R_{yx}^{(5f)}$ (d) at $T = 10$ K. Fitting curves (gray lines) are produced on the basis of the spin-orbit-torque model (see main text and Supplemental Material [57] for details). (e) Schematic illustrations of the models for understanding mechanisms of nonlinear Hall effects: (i) oscillation of magnetization by a damping-like spin-orbit torque and (ii) deflection of conduction electrons by vector and scalar spin chiralities. (f) Comparison of the respective maximum values of $R_{yx}^{(nf)}$ ($n = 1-7$) at $T = 10$ K. No clear signals of forth- and sixth-harmonics are detected around zero magnetic field. (Also see Supplemental Material [57], Fig. S4.)

the proportionality with respect to M_z . A hysteresis loop is observed in the second-harmonic resistance, which is characterized by a pronounced peak around zero magnetic field and followed by the rapid attenuation in the fully polarized state above H_c . Other even-order harmonics are not detected around zero magnetic field (Supplemental Material [57], Fig. S4). On the other hand, the third- and fifth-order harmonic resistances exhibit H_{out} -dependence profiles resembling those of $R_{yx}^{(1f)}$, albeit showing nonmonotonic behaviors below H_c .

First examining an overall trend, we find that the second-order harmonic resistance becomes pronounced below H_c , while the odd-order harmonics gradually develop with increasing H and reach their maxima above H_c . These contrasting behaviors between even and odd orders can be comprehensively rationalized within the framework where the ac current induces oscillating motions of the background magnetization via the SOT mechanism. When the in-plane M is tilted by an angle θ in the presence of H_{out} , and this orientation is further oscillated by an angle $\Delta\theta$ due to the dampinglike SOT [inset (i) of Fig. 4(e)], the anomalous Hall resistance can be extended to higher orders of I in the

following way:

$$R_{yx} = R_A M_z = R_A M \sin(\theta + \Delta\theta)$$

$$\approx R_A M \sin\theta + c R_A M \cos\theta \cdot I - \frac{c^2}{2} R_A M \sin\theta \cdot I^2 + \dots$$
(4)

Here we assume the linear relationship $\Delta\theta \approx cI$ in addition to the approximation by the Taylor series. (R_A is the anomalous Hall coefficient and c is a coefficient representing an efficiency of SOT [Supplemental Material [57], Fig. S4].) As evident from the correspondence between this equation (Eq. 4) and the definition of $R_{yx}^{(n)}$ (Eq. 1), the even-order $R_{yx}^{(n)}$ is proportional to the in-plane component of M , whereas the odd-order $R_{yx}^{(n)}$ is proportional to the out-of-plane component of M . Namely,

$$R_{yx}^{(nf)} \propto M \cos\theta \quad \text{for even } n, \quad (5)$$

$$R_{yx}^{(nf)} \propto M \sin\theta \quad \text{for odd } n. \quad (6)$$

This model effectively captures the general behaviors of all higher-order harmonic resistances. [See gray fitting curves in Figs. 4(b)–4(d) and also see Supplemental Material [57] for the detailed fitting curves.] However, there is discernible variation in the fitting coefficient c among different orders n , particularly the reduced c for reproducing $R_{yx}^{(2f)}$ (Supplemental Material [57], Fig. S4). Ideally, the estimated values of c should remain consistent, as the magnetization oscillation amplitude is uniquely determined. First, the modest discrepancy in the fitting coefficients for the odd-order $R_{yx}^{(nf)}$ suggests the necessity to extend the relationship between $\Delta\theta$ and I to higher orders (i.e., $\Delta\theta \approx cI + c'I^2 + c''I^3 + \dots$) and improve the approximation accuracy. On the other hand, the significant reduction in c for $R_{yx}^{(2f)}$ may be ascribed to the existence of multiple domains with different in-plane magnetization directions. There occurs strong cancellation between the contributions from the domains with oppositely polarized background magnetization. Only an uncompensated $R_{yx}^{(2f)}$, which appears as the reduction of c , survives as a result of an accidental imbalance of the magnetic domain population. The same thing happens to other even-order $R_{yx}^{(nf)}$, which are undetectably small (Fig. 4(f) and Supplemental Material [57], Fig. S4).

Next we focus on the nonmonotonic profiles of $R_{yx}^{(nf)}$ that result in the discrepancies between the measured $R_{yx}^{(nf)}$ and the fitting curves derived from the above model [Figs. 4(b)–4(d)]. It is highly plausible that these $R_{yx}^{(nf)}$ anomalies are associated with the SkB formation, as they show up exclusively below H_c . One possible microscopic origin could be asymmetric scatterings of the conduction electrons by the noncollinear spin structures [84–86]. On the basis of the symmetry argument, the higher-order nonlinear Hall effects are indeed expressed using vector and/or scalar spin chiralities as descriptors of the spin noncollinearity [Fig. 4(e)]. Given the symmetry of the heterochiral FeSi thin film (i.e., D_3 symmetry) and $SO(3)$ spin rotational symmetry, the nonlinear Hall effects bear proportionate relationships to the scalar spin

chirality, as is the case of the topological Hall effect:

$$\sigma_{xy}^{(n)} \propto \int \mathbf{S}(\mathbf{r}) \cdot [\partial_x \mathbf{S}(\mathbf{r}) \times \partial_y \mathbf{S}(\mathbf{r})] dx dy \quad \text{for all } n. \quad (7)$$

Here, $\sigma_{xy}^{(n)}$ is the n th-order Hall conductivity that causes Hall current in response to the n th power of the input electric field, namely, $J_y^{(n)} = \sigma_{xy}^{(n)}(E_x)^n$. In fact, $R_{yx}^{(3f)}$ profiles show little current dependence (Supplemental Material [57], Fig. S5), ensuring consistency with the asymmetric scattering mechanism, rather than with the effects of the emergent electromagnetic fields [76,87,88] or emergent induction [89,90] due to the current-induced motion of SkBs.

However, there is a peculiar structure in $R_{yx}^{(5f)}$, which remains unexplained by the asymmetric scattering mechanism. According to Eq. (7), the Hall signals resulting from asymmetric scattering are expected to display a similar H dependence over all orders n , since they are directly correlated with the scalar spin chirality, i.e., the noncollinearity of the spin structure. Indeed, $R_{yx}^{(2f)}$ and $R_{yx}^{(3f)}$ exhibit broad dip structures, seemingly reflecting the H dependence of SkB density as expected. In contrast, a sharp anomaly appears around H_c in $R_{yx}^{(5f)}$, representing the discrepancy with the present model. The anomaly in $R_{yx}^{(5f)}$ could potentially originate from enhanced skew scattering due to prominent spin fluctuations upon the collapse of SkBs [91]. The development of a comprehensive theory on nonlinear transport phenomena in noncollinear spin structures is highly desirable.

IV. CONCLUSION

We have realized the formation of SkBs at the quasi-2D ferromagnetic surface state of FeSi by leveraging the SOC

proximity of the adjacent Pt layer. The SkBs are strongly pinned by the structural disorders, resulting in their polydispersity or polymorphism and the greatly enhanced depinning threshold $J_c \approx 1.7 \times 10^{11}$ A/m². The strong pinning effect preserves the assembled structure of SkBs even at high current densities below J_c , enabling the access to the regime where prominent nonlinear responses show up. Consequently, we have identified the higher-order nonlinear Hall resistances $R_{yx}^{(n)}$ ($2 \leq n \leq 7$) with the characteristic H dependencies. These nonlinear Hall resistances comprise (i) the primary contribution from the magnetization dynamics due to SOT and (ii) the nontrivial Hall effects related to the noncollinearity inherent in the topological spin textures. The latter effect may stem from the asymmetric electron scattering by the scalar spin chirality, behaving as nonlinear extensions of the topological Hall effect. The observed rich profiles of nonlinear Hall effects may experimentally exemplify the theoretical model in the initial proposal for utilizing skyrmions in reservoir computing [80,81]. The present study also demonstrates the potential for tailored manipulation of various quantum functionalities via the interface engineering of the topological surface state of FeSi, in analogy to the van der Waals heterostructures.

ACKNOWLEDGMENTS

We thank X. Z. Yu, L. Peng, F. S. Yasin, and S. Mori for experimental supports and J. Masell for fruitful discussions. This work was supported by JSPS KAKENHI (Grants No. 22K18965, No. 23H04017, No. 23H05431, No. 23H05462, No. 24H00417, and No. 24H01652), JST FOREST (Grant No. JPMJFR2038), JST CREST (Grants No. JPMJCR1874 and No. JPMJCR23O3), the Mitsubishi Foundation, and the special fund of the Institute of Industrial Science, The University of Tokyo.

-
- [1] M. N. Baibich, J. M. Broto, A. Fert, F. Nguyen Van Dau, F. Petroff, P. Etienne, G. Creuzet, A. Friederich, and J. Chazelas, *Phys. Rev. Lett.* **61**, 2472 (1988).
 - [2] G. Binasch, P. Grünberg, F. Saurenbach, and W. Zinn, *Phys. Rev. B* **39**, 4828(R) (1989).
 - [3] S. S. P. Parkin, *Annu. Rev. Mater. Sci.* **25**, 357 (1995).
 - [4] D. L. Cortie, G. L. Causer, K. C. Rule, H. Fritzsche, W. Kreuzpaintner, and F. Klose, *Adv. Funct. Mater.* **30**, 1901414 (2020).
 - [5] Y. Tokura, K. Yasuda, and A. Tsukazaki, *Nat. Rev. Phys.* **1**, 126 (2019).
 - [6] B. A. Bernevig, C. Felser, and H. Beidenkopf, *Nature (London)* **603**, 41 (2022).
 - [7] L. Šmejkal, Y. Mokrousov, B. Yan, and A. H. MacDonald, *Nat. Phys.* **14**, 242 (2014).
 - [8] M. Z. Hasan, G. Chang, I. Belopolski, G. Bian, S.-Y. Xu, and J.-X. Yin, *Nat. Rev. Mater.* **6**, 784 (2021).
 - [9] A. K. Geim and I. V. Grigorieva, *Nature (London)* **499**, 419 (2013).
 - [10] C. Gong and X. Zhang, *Science* **363**, eaav4450 (2019).
 - [11] M. Gibertini, M. Koperski, A. F. Morpurgo, and K. S. Novoselov, *Nat. Nanotechnol.* **14**, 408 (2019).
 - [12] K. F. Mak, J. Shan, and D. C. Ralph, *Nat. Rev. Phys.* **1**, 646 (2019).
 - [13] B. Huang, M. A. McGuire, A. F. May, D. Xiao, P. Jarillo-Herrero, and X. Xu, *Nat. Mater.* **19**, 1276 (2020).
 - [14] C.-Z. Chang, J. Zhang, X. Feng, J. Shen, Z. Zhang, M. Guo, K. Li, Y. Ou, P. Wei, L.-L. Wang, Z.-Q. Ji, Y. Feng, S. Ji, X. Chen, J. Jia, X. Dai, Z. Fang, S.-C. Zhang, K. He, Y. Wang *et al.*, *Science* **340**, 167 (2013).
 - [15] Y. Deng, Y. Yu, M. Z. Shi, Z. Guo, Z. Xu, J. Wang, X. H. Chen, and Y. Zhang, *Science* **367**, 895 (2020).
 - [16] M. Serlin, C. L. Tschirhart, H. Polshyn, Y. Zhang, J. Zhu, K. Watanabe, T. Taniguchi, L. Balents, and A. F. Young, *Science* **367**, 900 (2020).
 - [17] H. Park, J. Cai, E. Anderson, Y. Zhang, J. Zhu, X. Liu, C. Wang, W. Holtzmann, C. Hu, Z. Liu, T. Taniguchi, K. Watanabe, J.-H. Chu, T. Cao, L. Fu, W. Yao, C.-Z. Chang, D. Cobden, D. Xiao, and X. Xu, *Nature (London)* **622**, 74 (2023).
 - [18] D. Zhong, K. L. Seyler, X. Linpeng, R. Cheng, N. Sivadas, B. Huang, E. Schmidgall, T. Taniguchi, K. Watanabe, M. A. McGuire, W. Yao, D. Xiao, K.-M. C. Fu, and X. Xu, *Sci. Adv.* **3**, e1603113 (2017).

- [19] K. L. Seyler, D. Zhong, B. Huang, X. Linpeng, N. P. Wilson, T. Taniguchi, K. Watanabe, W. Yao, D. Xiao, M. A. McGuire, K.-M. C. Fu, and X. Xu, *Nano Lett.* **18**, 3823 (2018).
- [20] A. Manchon, H. C. Koo, J. Nitta, S. M. Frolov, and R. A. Duine, *Nat. Mater.* **14**, 871 (2015).
- [21] A. Soumyanarayanan, N. Reyren, A. Fert, and C. Panagopoulos, *Nature (London)* **539**, 509 (2016).
- [22] F. Hellman, A. Hoffmann, Y. Tserkovnyak, G. S. D. Beach, E. E. Fullerton, C. Leighton, A. H. MacDonald, D. C. Ralph, D. A. Arena, H. A. Durr, P. Fischer, J. Grollier, J. P. Heremans, T. Jungwirth, A. V. Kimel, B. Koopmans, I. N. Krivorotov, S. J. May, A. K. Petford-Long, J. M. Rondinelli *et al.*, *Rev. Mod. Phys.* **89**, 025006 (2017).
- [23] G. Bihlmayer, P. Noël, D. V. Vyalikh, E. V. Chulkov, and A. Manchon, *Nat. Rev. Phys.* **4**, 642 (2022).
- [24] E. I. Rashba, *Sov. Phys. Solid State* **2**, 1109 (1960).
- [25] I. Dzyaloshinsky, *J. Phys. Chem. Solids* **4**, 241 (1958).
- [26] T. Moriya, *Phys. Rev.* **120**, 91 (1960).
- [27] R. Wiesendanger, *Nat. Rev. Mater.* **1**, 16044 (2016).
- [28] A. Fert, N. Reyren, and V. Cros, *Nat. Rev. Mater.* **2**, 17031 (2017).
- [29] A. N. Bogdanov and C. Panagopoulos, *Nat. Rev. Phys.* **2**, 492 (2020).
- [30] V. M. Edelstein, *Solid State Commun.* **73**, 233 (1990).
- [31] K. Garello, I. M. Miron, C. O. Avci, F. Freimuth, Y. Mokrousov, S. Blügel, S. Auffret, O. Boulle, G. Gaudin, and P. Gambardella, *Nat. Nanotechnol.* **8**, 587 (2013).
- [32] A. Manchon, J. Železný, I. M. Miron, T. Jungwirth, J. Sinova, A. Thiaville, K. Garello, and P. Gambardella, *Rev. Mod. Phys.* **91**, 035004 (2019).
- [33] T. Yokouchi, N. Kanazawa, A. Kikkawa, D. Morikawa, K. Shibata, T. Arima, Y. Taguchi, F. Kagawa, and Y. Tokura, *Nat. Commun.* **8**, 866 (2017).
- [34] Y. Tokura and N. Nagaosa, *Nat. Commun.* **9**, 3740 (2018).
- [35] A. Neubauer, C. Pfleiderer, B. Binz, A. Rosch, R. Ritz, P. G. Niklowitz, and P. Böni, *Phys. Rev. Lett.* **102**, 186602 (2009).
- [36] M. Lee, W. Kang, Y. Onose, Y. Tokura, and N. P. Ong, *Phys. Rev. Lett.* **102**, 186601 (2009).
- [37] F. Jonietz, S. Mühlbauer, C. Pfleiderer, A. Neubauer, W. Münzer, A. Bauer, T. Adams, R. Georgii, P. Böni, R. A. Duine, K. Everschor, M. Garst, and A. Rosch, *Science* **330**, 1648 (2010).
- [38] S. Woo, K. Litzius, B. Krüger, M.-Y. Im, L. Caretta, K. Richter, M. Mann, A. Krone, R. M. Reeve, M. Weigand, P. Agrawal, I. Lamesh, M.-A. Mawass, P. Fischer, M. Kläui, and G. S. D. Beach, *Nat. Mater.* **15**, 501 (2016).
- [39] Y. Ohtsuka, N. Kanazawa, M. Hirayama, A. Matsui, T. Nomoto, R. Arita, T. Nakajima, T. Hanashima, V. Ukleev, H. Aoki, M. Mogi, K. Fujiwara, A. Tsukazaki, M. Ichikawa, M. Kawasaki, and Y. Tokura, *Sci. Adv.* **7**, eabj0498 (2021).
- [40] T. Hori, N. Kanazawa, M. Hirayama, K. Fujiwara, A. Tsukazaki, M. Ichikawa, M. Kawasaki, and Y. Tokura, *Adv. Mater.* **35**, 2206801 (2023).
- [41] L. F. Mattheiss and D. R. Hamann, *Phys. Rev. B* **47**, 13114 (1993).
- [42] Y. Fang, S. Ran, W. Xie, S. Wang, Y. S. Meng, and M. B. Maple, *Proc. Natl. Acad. Sci. USA* **115**, 8558 (2018).
- [43] B. Yang, M. Uphoff, Y.-Q. Zhang, J. Reichert, A. P. Seitsonen, A. Bauer, C. Pfleiderer, and J. V. Barth, *Proc. Natl. Acad. Sci. USA* **118**, e2021203118 (2021).
- [44] Y. S. Eo, K. Avers, J. A. Horn, H. Yoon, S. R. Saha, A. Suarez, M. S. Fuhrer, and J. Paglione, *Appl. Phys. Lett.* **122**, 233102 (2023).
- [45] J. Zak, *Phys. Rev. Lett.* **62**, 2747 (1989).
- [46] R. Resta, *Ferroelectrics* **136**, 51 (1992).
- [47] R. D. King-Smith and D. Vanderbilt, *Phys. Rev. B* **47**, 1651 (1993).
- [48] D. Vanderbilt and R. D. King-Smith, *Phys. Rev. B* **48**, 4442 (1993).
- [49] S. Changdar, S. Aswartham, A. Bose, Y. Kushnirenko, G. Shipunov, N. C. Plumb, M. Shi, A. Narayan, B. Büchner, and S. Thirupathiah, *Phys. Rev. B* **101**, 235105 (2020).
- [50] Z. Schlesinger, Z. Fisk, H.-T. Zhang, M. B. Maple, J. DiTusa, and G. Aeppli, *Phys. Rev. Lett.* **71**, 1748 (1993).
- [51] C. Fu and S. Doniach, *Phys. Rev. B* **51**, 17439 (1995).
- [52] V. I. Anisimov, S. Y. Ezhov, I. S. Elfimov, I. V. Solov'ev, and T. M. Rice, *Phys. Rev. Lett.* **76**, 1735 (1996).
- [53] J. M. Tomczak, K. Haule, and G. Kotliar, *Proc. Natl. Acad. Sci. USA* **109**, 3243 (2012).
- [54] S. Heinze, K. von Bergmann, M. Menzel, J. Brede, A. Kubetzka, R. Wiesendanger, G. Bihlmayer, and S. Blügel, *Nat. Phys.* **7**, 713 (2011).
- [55] N. Romming, C. Hanneken, M. Menzel, J. E. Bickel, B. Wolter, K. von Bergmann, A. Kubetzka, and R. Wiesendanger, *Science* **341**, 636 (2013).
- [56] H. von Känel, K. A. Mäder, E. Müller, N. Onda, and H. Sirringhaus, *Phys. Rev. B* **45**, 13807(R) (1992).
- [57] See Supplemental Material at <http://link.aps.org/supplemental/10.1103/PhysRevMaterials.8.044407> for characterization of the sample, longitudinal resistance, current-pulse dependence of the development of magnetic-domain pattern, and dataset of all higher-harmonic Hall resistances.
- [58] P. Bruno, *Phys. Rev. B* **39**, 865(R) (1989).
- [59] G. van der Laan, *J. Phys.: Condens. Matter* **10**, 3239 (1998).
- [60] K. Everschor-Sitte, J. Masell, R. M. Reeve, and M. Kläui, *J. Appl. Phys.* **124**, 240901 (2018).
- [61] H. Yang, A. Thiaville, S. Rohart, A. Fert, and M. Chshiev, *Phys. Rev. Lett.* **115**, 267210 (2015).
- [62] A. Belabbes, G. Bihlmayer, F. Bechstedt, S. Blügel, and A. Manchon, *Phys. Rev. Lett.* **117**, 247202 (2016).
- [63] Y. Yoshida, S. Schröder, P. Ferriani, D. Serrate, A. Kubetzka, K. von Bergmann, S. Heinze, and R. Wiesendanger, *Phys. Rev. Lett.* **108**, 087205 (2012).
- [64] Y. A. Kharkov, O. P. Sushkov, and M. Mostovoy, *Phys. Rev. Lett.* **119**, 207201 (2017).
- [65] B. Göbel, A. Mook, J. Henk, I. Mertig, and O. A. Tretiakov, *Phys. Rev. B* **99**, 060407(R) (2019).
- [66] J. Vijayakumar, Y. Li, D. Bracher, C. W. Barton, M. Horisberger, T. Thomson, J. Miles, C. Moutafis, F. Nolting, and C. A. F. Vaz, *Phys. Rev. Appl.* **14**, 054031 (2020).
- [67] K. Ohara, X. Zhang, Y. Chen, S. Kato, J. Xia, M. Ezawa, O. A. Tretiakov, Z. Hou, Y. Zhou, G. Zhao, J. Yang, and X. Liu, *Nano Lett.* **22**, 8559 (2022).
- [68] I. Gross, W. Akhtar, A. Hrabec, J. Sampaio, L. J. Martínez, S. Chouaieb, B. J. Shields, P. Maletinsky, A. Thiaville, S. Rohart, and V. Jacques, *Phys. Rev. Mater.* **2**, 024406 (2018).
- [69] C. Reichhardt, C. J. O. Reichhardt, and M. V. Milošević, *Rev. Mod. Phys.* **94**, 035005 (2022).

- [70] R. Gruber, J. Zázvorka, M. A. Brems, D. R. Rodrigues, T. Dohi, N. Kerber, B. Seng, M. Vafaee, K. Everschor-Sitte, P. Virnau, and M. Kläui, *Nat. Commun.* **13**, 3144 (2022).
- [71] X. Z. Yu, N. Kanazawa, W. Z. Zhang, T. Nagai, T. Hara, K. Kimoto, Y. Matsui, Y. Onose, and Y. Tokura, *Nat. Commun.* **3**, 988 (2012).
- [72] W. Jiang, P. Upadhyaya, W. Zhang, G. Yu, M. B. Jungfleisch, F. Y. Fradin, J. E. Pearson, Y. Tserkovnyak, K. L. Wang, O. Heinonen, S. G. E. te Velthuis, and A. Hoffmann, *Science* **349**, 283 (2015).
- [73] W. Jiang, X. Zhang, G. Yu, W. Zhang, X. Wang, M. B. Jungfleisch, J. E. Pearson, X. Cheng, O. Heinonen, K. L. Wang, Y. Zhou, A. Hoffmann, and S. G. E. te Velthuis, *Nat. Phys.* **13**, 162 (2017).
- [74] A. Hrabec, J. Sampaio, M. Belmeguenai, I. Gross, R. Weil, S. M. Chérif, A. Stashkevich, V. Jacques, A. Thiaville, and S. Rohart, *Nat. Commun.* **8**, 15765 (2017).
- [75] S. Woo, K. M. Song, X. Zhang, Y. Zhou, M. Ezawa, X. Liu, S. Finizio, J. Raabe, N. J. Lee, S. Kim, S.-Y. Park, Y. Kim, J.-Y. Kim, D. Lee, O. Lee, J. W. Choi, B.-C. Min, H. C. Koo, and J. Chang, *Nat. Commun.* **9**, 959 (2018).
- [76] J. Zang, M. Mostovoy, J. H. Han, and N. Nagaosa, *Phys. Rev. Lett.* **107**, 136804 (2011).
- [77] S. Hoshino and N. Nagaosa, *Phys. Rev. B* **97**, 024413 (2018).
- [78] F. Ando, Y. Miyasaka, T. Li, J. Ishizuka, T. Arakawa, Y. Shiota, T. Moriyama, Y. Yanase, and T. Ono, *Nature (London)* **584**, 373 (2020).
- [79] M. Nadeem, M. S. Fuhrer, and X. Wang, *Nat. Rev. Phys.* **5**, 558 (2023).
- [80] D. Prychynenko, M. Sitte, K. Litzius, B. Krüger, G. Bourianoff, M. Kläui, J. Sinova, and K. Everschor-Sitte, *Phys. Rev. Appl.* **9**, 014034 (2018).
- [81] D. Pinna, G. Bourianoff, and K. Everschor-Sitte, *Phys. Rev. Appl.* **14**, 054020 (2020).
- [82] J. Grollier, D. Querlioz, K. Y. Camsari, K. Everschor-Sitte, S. Fukami, and M. D. Stiles, *Nat. Electron.* **3**, 360 (2020).
- [83] O. Lee, R. Msiska, M. A. Brems, M. Kläui, H. Kurebayashi, and K. Everschor-Sitte, *Appl. Phys. Lett.* **122**, 260501 (2023).
- [84] H. Ishizuka and N. Nagaosa, *Sci. Adv.* **4**, eaap9962 (2018).
- [85] H. Ishizuka and N. Nagaosa, *Nat. Commun.* **11**, 2986 (2020).
- [86] C. Schütte and M. Garst, *Phys. Rev. B* **90**, 094423 (2014).
- [87] G. Volovik, *J. Phys. C* **20**, L83 (1987).
- [88] T. Schulz, R. Ritz, A. Bauer, M. Halder, M. Wagner, C. Franz, C. Pfleiderer, K. Everschor, M. Garst, and A. Rosch, *Nat. Phys.* **8**, 301 (2012).
- [89] N. Nagaosa, *Jpn. J. Appl. Phys.* **58**, 120909 (2019).
- [90] T. Yokouchi, F. Kagawa, M. Hirschberger, Y. Otani, N. Nagaosa, and Y. Tokura, *Nature (London)* **586**, 232 (2020).
- [91] Y. Fujishiro, N. Kanazawa, R. Kurihara, H. Ishizuka, T. Hori, F. S. Yasin, X. Z. Yu, A. Tsukazaki, M. Ichikawa, M. Kawasaki, N. Nagaosa, M. Tokunaga, and Y. Tokura, *Nat. Commun.* **12**, 317 (2021).